Letter | Editors' Suggestion

Frequency-dependent phonon-mediated unidirectional magnetoresistance in a metal on an insulator with highly nonequilibrium magnons

Sean E. Sullivan [1,*,†], Hwijong Lee [1,*,‡], Annie Weathers,[2,§] and Li Shi [1,2,#]

[1]*Materials Science and Engineering Program, The University of Texas at Austin, Austin, Texas 78712, USA*

[2]*Department of Mechanical Engineering, The University of Texas at Austin, Austin, Texas 78712, USA*

(Received 9 March 2021; revised 28 March 2023; accepted 29 March 2023; published 28 April 2023)

Heavy-metal (HM)/magnet bilayers host many magnetoresistance (MR) and spin caloritronic effects. Here, we show that the spin Peltier effect and electron-phonon scattering produce much larger unidirectional MR of an HM on a magnetic insulator than existing theories that neglect the interplay between MR and spin caloritronic effects. By accounting for local nonequilibrium in both the magnon chemical potential and temperature, our analytical model attributes the observed frequency dependence of the spin Peltier MR and the spin Seebeck effect to the reduction of the thermal penetration depth, which approaches the 1-μm-scale magnon spin-diffusion length at high frequencies.

DOI: 10.1103/PhysRevB.107.L140412

A panoply of magnetoresistance (MR) [1–3] and spin caloritronic effects [4–7] has emerged in heterostructures comprising a heavy metal (HM) and a ferromagnetic metal or insulator (FM or FI). These effects enable the conversion among electrical, thermal, and magnetic signals for information processing and energy conversion. Compared to the established mechanisms for anisotropic magnetoresistance [8] and giant magnetoresistance (GMR) [9,10], the physics behind these MR effects in HM/FM and HM/FI heterostructures is nuanced. A previous experiment [1] observed a minimum in the resistance of an HM film on an FI when the in-plane magnetization ($\boldsymbol{M}$) of the FI was made perpendicular to the electric current ($\boldsymbol{I}$) in the metal. Dubbed as a spin Hall magnetoresistance (SMR), this minimum has been attributed to the interface reflection of the spin current generated by the spin Hall effect (SHE) to produce an additional charge-current ($\boldsymbol{I}$) component via the inverse SHE (ISHE) [11–14] when the net spin polarization ($\boldsymbol{\sigma}$) in the HM is collinear with $\boldsymbol{M}$ [1]. HM/FM bilayers further exhibit an MR that changes sign upon a reversal of either $\boldsymbol{M}$ or $\boldsymbol{I}$ [2]. Referred to as a unidirectional MR (UMR), this breaking of time-reversal symmetry has been explained based on spin-dependent electron-electron scattering analogous to current-in-plane GMR, except that the role of the FM polarizer in GMR is replaced by the SHE in the normal metal [2,15,16]. Meanwhile, a UMR has also been attributed to electron-magnon scattering that flips the HM electron spin and increases or decreases the magnetization and longitudinal resistance of the FM depending on the $\boldsymbol{M}$ direction [15,17]. A theoretical study investigated the electron-magnon scattering mechanism and predicted a small magnonic UMR on the order of 10^{-8} at a current density $j = 1 \times 10^{12}\,\mathrm{A\,m^{-2}}$ in Pt on yttrium iron garnet (YIG) [18]. In this prototypical HM/FI heterostructure, the interfacial spin flux (J_s^i) driven by the SHE in the HM creates or annihilates magnons in the FI depending on the $\boldsymbol{M}$ direction. The resultant magnon accumulation produces additional components, which are linear and quadratic functions of $\boldsymbol{I}$, to both J_s^i and the longitudinal electric field (E) caused by the ISHE. The quadratic term results in a magnonic UMR that is linear with $\boldsymbol{I}$ [18].

In parallel, the spin Seebeck effect (SSE) has been explained based on the ISHE-mediated conversion of a thermally driven J_s^i into an in-plane E field in a metal on an FI [4]. Conversely, temperature modulation from the spin Peltier effect (SPE) is attributed to the heat transported by an interfacial spin current injected by the SHE from an in-plane electric current [5]. Often neglected in the studies of various MR effects in the same heterostructures, the SPE and SSE contributions are controlled by coupled spin and heat-transport properties of nonequilibrium magnons [5,19].

Here, we report measurements of a UMR on the order of 10^{-6} in a Pt/YIG heterostructure, several orders of magnitude larger than previously predicted [18] or measured [20,21]. We attribute this UMR to a spin Peltier MR (SPMR). Without changing the direction of the J_s^i injected by the SHE, an $\boldsymbol{M}$ reversal flips the sign of the SPE heat current because of a switching between magnon creation and annihilation by the J_s^i. The Pt temperature is thus either cooled or heated by the SPE depending on the $\boldsymbol{M}$ direction. Electron-phonon coupling causes the Pt resistivity to vary with its temperature that depends on the $\boldsymbol{M}$ direction. The magnitude of this UMR agrees with the past measured SPE modulation of the Pt temperature [6]. We consider both the magnon chemical potential and magnon-phonon temperature nonequilibrium in an analytical solution of the coupled spin, charge, and heat-transport

*These authors contributed equally to this work.

†Present address: memQ, Inc., Chicago, Illinois 60637, USA.

‡Present address: Center for Integrated Nanotechnologies (CINT), Sandia National Laboratories, Albuquerque, New Mexico 87185, USA.

§Present address: MIT Lincoln Laboratory, Lexington, Massachusetts 02421, USA.

#Corresponding author: lishi@mail.utexas.edu

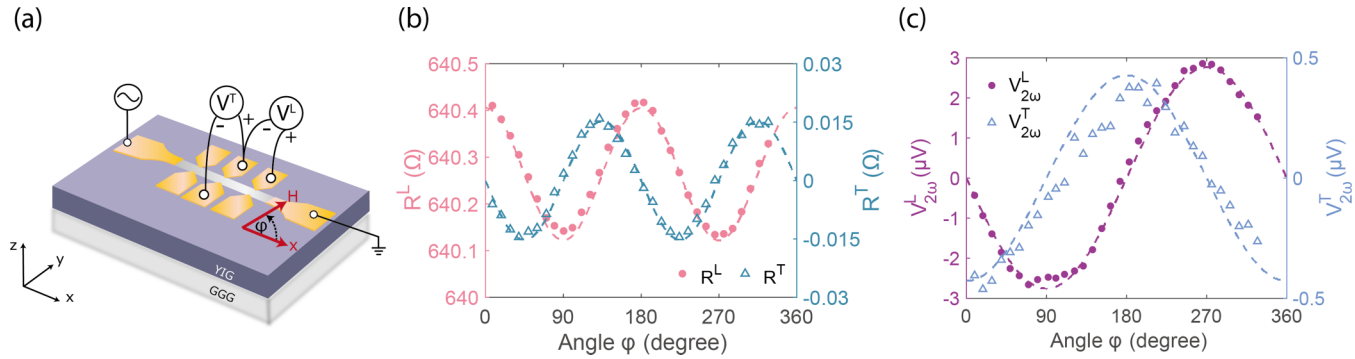

FIG. 1. (a) Schematic illustration of the longitudinal resistance (R^{L}) and Hall resistance (R^{T}) measurements with two lock-in amplifiers. The frequency and rms amplitude of the sinusoidal excitation current are $\omega/2\pi = 1017.1$ Hz and $I_\omega = 1$ mA, respectively. The $\boldsymbol{H}$ field is -20 mT. (b) Angular dependence of R^{L} and R^{T} measured as the ratios between the corresponding in-phase (X) 1ω voltages ($V^{\mathrm{L}}_{\omega,X}$ and $V^{\mathrm{T}}_{\omega,X}$) and I_ω. (c) Angular dependence of the out-of-phase (Y), 2ω components of the longitudinal ($V^{\mathrm{L}}_{2\omega,Y}$) and transverse ($V^{\mathrm{T}}_{2\omega,Y}$) voltages. Lines are model fitting to the measurement data (symbols).

equations. Our analysis is able to explain the observed frequency dependence of the SPMR and the reciprocal SSE based on the interplay among the frequency-dependent thermal penetration depth (Λ), a 1-μm-scale magnon spin-diffusion length (λ), and a magnon-phonon thermalization length (l_{mp}) below 300 nm [22–25].

Our samples comprise 5.8-nm-thick Pt Hall bar structures on 3-μm-thick YIG film on a $Gd_3Ga_5O_{12}$ (GGG) substrate, which was kept at room temperature. When a sinusoidal current with a root-mean-square (rms) amplitude $I_\omega = 1$ mA is injected at a frequency $\frac{\omega}{2\pi} = 1017.2$ Hz, the longitudinal resistance (R^L) and transverse Hall resistance (R^T) of the Pt line measured with a lock-in amplifier at the 1ω frequency can be fitted with $R^L = R_0 + \Delta R^L \cos 2\varphi$ and $R^T = \Delta R^T \sin 2\varphi$, respectively, with φ being the angle between the applied magnetic field H and the current flow direction [see Figs. 1(a) and 1(b)], $\frac{\Delta R^L}{R_0} = 2.21 \times 10^{-4}$, and $\frac{\Delta R^L}{\Delta R^T} = \frac{L}{w_H} = 9.3$, with $L = 290\,\mu$m being the distance between the two longitudinal voltage probes and $w_H = 31.2\,\mu$m being the gap width between the two Hall voltage probes. Both the angular dependence and the magnitudes are consistent with prior SMR measurements [1] and can be used to calculate the real part of the spin-mixing conductance (g_r) as $1.1 \times 10^{14}\ \Omega^{-1}\,\mathrm{m}^{-2}$ [23,26,27].

Because Joule heating is modulated at the 2ω frequency, the transverse Hall probes detect an out-of-phase (Y) 2ω component of the thermally driven SSE voltage that can be fitted with $V^T_{2\omega,Y} = -\Delta V^T_{2\omega} \cos\varphi$ [see Fig. 1(c)]. In comparison, the 2ω component in the measured longitudinal voltage drop can be fitted with $V^L_{2\omega,Y} = -\Delta V^L_{2\omega} \sin\varphi$. Although the angular dependence agrees with the SSE, at low frequencies the $\frac{\Delta V^L_{2\omega}}{\Delta V^T_{2\omega}} = 6.45$ ratio differs considerably from $\frac{L}{w_H} = 9.3$, indicating the presence of additional contributions to $\Delta V^L_{2\omega}$ besides the SSE voltage that is proportional to the distance between the voltage probes. As the predicted magnonic UMR ($\mathcal{U}$) is a linear function of the current [18], it contributes an amount $\mathcal{U} R_0 I_\omega$ to $\Delta V_{2\omega}$. At the current-density modulation amplitude $j_\omega = 4.7 \times 10^9\ \mathrm{A\,m^{-2}}$ used in this measurement, however, the predicted $\mathcal{U}$ is five orders of magnitude smaller than the observed UMR $= (\Delta V^L_{2\omega} - \frac{L}{w_H}\Delta V^T_{2\omega})/I_\omega = 1.7 \times 10^{-6}$, where $\frac{L}{w_H}\Delta V^T_{2\omega}$ is the expected SSE contribution to $\Delta V^L_{2\omega}$. This geometric scaling approach is similar to prior extraction of a UMR in thin HM/FM bilayers [2], except that the magnetoresistive, anomalous, and planar Hall effects in the FM [15] are absent in the FI here.

To reduce the noise in the longitudinal measurements at high frequencies, we utilized a balanced circuit to nullify the large 1ω voltage component [see Fig. 2(a)]. Taking advantage of the device symmetry to reduce common mode noise, we inected the sinusoidal current through the central contacts and measured the longitudinal voltage as current flowed to both the left and right sides of the Pt line. Bridge-circuit analysis yields an SSE contribution to the measured $\Delta V^L_{2\omega,Y}$ as $\Delta V^L_{\mathrm{SSE},2\omega,Y} = \gamma(L_h/w_H)\Delta V^T_{2\omega,Y}$, where $L_h = 320\,\mu$m is the length of each half of the Pt line, and the additional factor γ depends on the resistances in the bridge circuit [28]. As shown in Fig. 2(b), the apparent difference ($\Delta V_{\mathrm{SPE},2\omega,Y}$) between the measured $\Delta V^L_{2\omega,Y}$ and the obtained SSE contribution can be converted to a change of the Pt line resistance due to the $\boldsymbol{M}$ reversal. At low frequencies, the obtained UMR increases linearly with the current [Fig. 2(c)] and reaches the same value of 1.7×10^{-6} at $j_\omega = 4.7 \times 10^9\ \mathrm{A\,m^{-2}}$ as the measurements from Fig. 1. As the $\Delta V^L_{2\omega}$ signals are not detectable in a Pt/GGG control sample [28], we rule out contributions from ordinary thermoelectric effects to the observed UMR in the Pt/YIG/GGG sample. In addition, we devised a lock-in Brillouin light-scattering measurement to verify the presence of a J^i_s that is modulated at the 1ω frequency, consistent with the SHE effect [28].

Several measurements of HM/FI heterostructures have found that the HM phonon temperature depends linearly on $\boldsymbol{I}$ when $\boldsymbol{M}$ and $\boldsymbol{\sigma}$ are collinear [5,6]. The observation has been attributed to the SPE, which was not accounted for in the prior UMR theories [18]. A change in the phonon temperature is expected to alter both the phonon-electron scattering rate and the resistivity of the Pt. If the observed UMR is attributed to such an SPMR, the Pt phonon temperature change due to the SPE would be $\langle \vartheta_{p,Pt,\,\omega} \rangle = \mathrm{UMR/TCR}$, where TCR is the temperature coefficient of resistance of the Pt. A linear fit of the calculated low frequency $\langle \vartheta_{p,Pt,\,\omega} \rangle$ with the j_ω in the Pt yields a slope of $4.5 \times 10^{-13}\ \mathrm{K\,m^2\,A^{-1}}$ [Fig. 2(c)], which is close to previous SPE measurement results [6,29]. In addition,

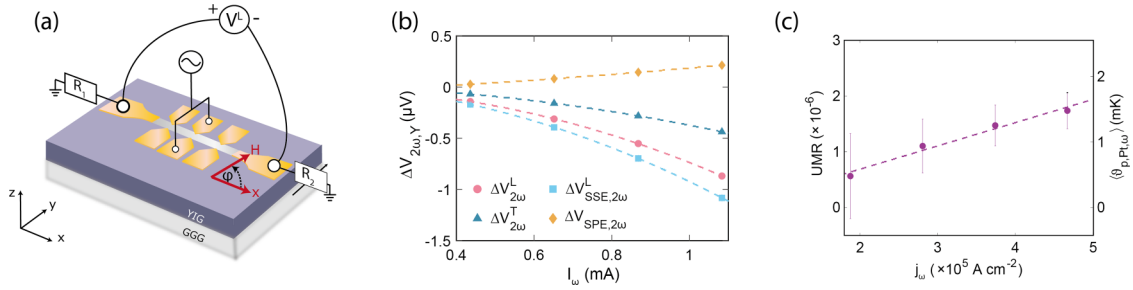

FIG. 2. (a) Schematic diagram of the longitudinal bridge measurement configuration. A precision resistor (R_1) and variable resistor (R_2) are used in a balanced circuit to nullify the 1ω component of the bridge voltage V^{L}. (b) Measured $\Delta V^{\mathrm{T}}_{2\omega,Y}$ at $\varphi = 180^\circ$ and $\Delta V^{\mathrm{L}}_{2\omega,Y}$ at $\varphi = -90^\circ$ as a function of the current modulation amplitudes at 50.17 Hz. Lines are quadratic fits to the data. (c) UMR (left axis) and equivalent Pt phonon temperature modulation (right axis) due to the SPE at $\phi = -90^\circ$ as a function of the current-density amplitude in the Pt at 50.17-Hz frequency. Dashed line is a linear fit of the data (symbols).

the sign of the calculated $\langle\vartheta_{p,Pt,\,\omega}\rangle$ is fully consistent with the SPE.

As $\omega/2\pi$ exceeds 10^4 Hz, the magnitudes of the Y [Fig. 3(a)] and X [Fig. 3(b)] components of the 2ω voltage signals decrease and increase with increasing ω, respectively, while the extracted X and Y components of the UMR and $\langle\vartheta_{p,Pt,\,\omega}\rangle$ begin to vary with frequency [see Fig. 3(c)]. With the measured $\langle\vartheta_{p,Pt,\,\omega}\rangle$ and $\Delta V^{T}_{2\omega}$ normalized by the low-frequency limit $\langle\vartheta_{p,Pt,\,\omega\to 0,X}\rangle$ and $\Delta V^{T}_{2\omega\to 0,Y}$ measured at $\omega/2\pi = 50.17$ Hz, the proposed SPE signal shows a similar frequency dependence as the SSE [Fig. 4(a)].

A recent two-temperature model [30] has used the frequency dependence of the thermal penetration depth Λ to explain the reported SSE signal roll-off at higher frequencies in thinner YIG films without invoking a hypothesis based on the thickness confinement effect on the magnon dispersion [31]. This model has not accounted for the magnon chemical potential (μ_m) [23,32], which appears as a thermodynamic property in addition to the magnon temperature because the magnon number density is approximately conserved inside the long spin-diffusion length. Here, we establish a model to account for both μ_m and the magnon-phonon temperature difference (ϑ_{m-p}) and obtain the following analytical solutions of their frequency-modulation components:

$$\hat{\vartheta}_{m-p} = \sum_{j=0,1,2} e_j \left[a_j \exp\left(\frac{z}{l_j}\right) + b_j \exp\left(\frac{-z}{l_j}\right)\right], \quad (1)$$

$$\hat{\mu}_m = \sum_{j=0,1,2} d_j \left[a_j \exp\left(\frac{z}{l_j}\right) + b_j \exp\left(\frac{-z}{l_j}\right)\right], \quad (2)$$

where the a_j and b_j coefficients are obtained from the boundary conditions, and e_j and d_j are determined by the phonon and magnon properties including the magnon conductivity (σ_m) and bulk spin coefficient (S_m). In addition, l_2 approaches the smaller value between l_{mp} and λ when the two are very different and S_m is small. In comparison, the other two length scales l_0 and l_1 follow Λ and $\max(l_{mp},\ \lambda)$, respectively, until an anticrossing behavior emerges in Fig. 4(b) when Λ is reduced to the latter. The anticrossing behavior is accompanied with the appearance of wavelike profiles in both the temperatures and μ_m (see Fig. S12), which results in a broad high-frequency peak in the calculated out-of-phase component of the frequency-dependent SPE and SSE signals [Fig. 4(a)]. As such features are absent in the frequency range

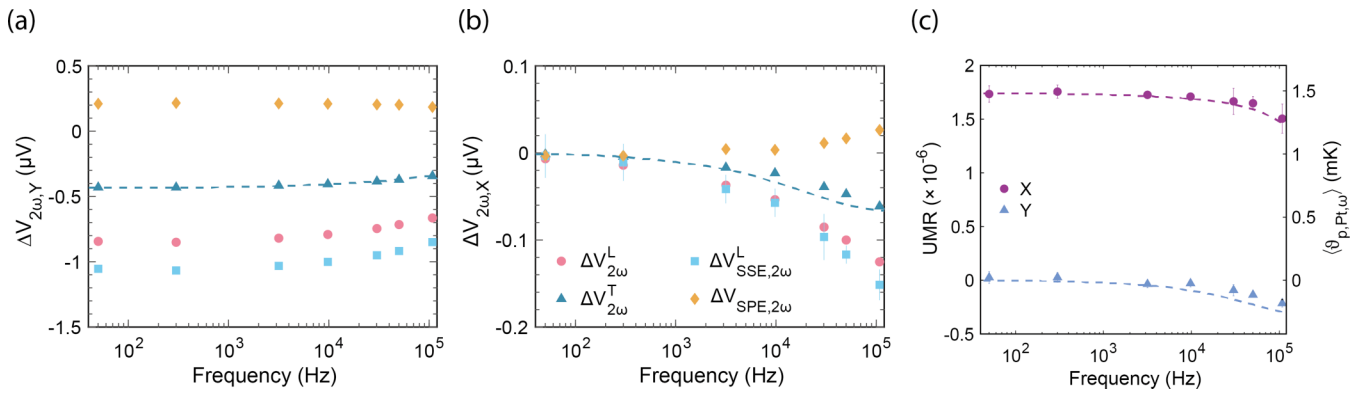

FIG. 3. Out-of-phase (a) and in-phase (b) components of the $\Delta V_{2\omega}$ (symbols) as a function of the frequency of the current modulation at 1.08-mA amplitude in the Pt line. In (a) and (b), $\Delta V^{T}_{2\omega}$ are compared with the analytical solutions with $\lambda = 830$ nm, $l_{mp} = 250$ nm, $\kappa_M = 0.1\,\mathrm{W m^{-1}\ K^{-1}}$, $\sigma_m = 1.85 \times 10^6\,\mathrm{S m^{-1}}$, $S_m = 63.5\,\mu\mathrm{V\,K^{-1}}$, and $S_s = 65.5\,\mu\mathrm{V\,K^{-1}}$. Legend in (b) is for both (a) and (b). Error bars indicate the statistical uncertainty with 95% confidence. (c) UMR (left axis) and equivalent Pt phonon temperature modulation (right axis) due to the SPE at $\phi = -90^\circ$ as a function of the current frequency at $4.7 \times 10^9\,\mathrm{A\,m^{-2}}$ current density. Dashed lines in (c) are obtained from the analytical solutions with the same parameters as those in (a) except that $S_m = 45.0\,\mu\mathrm{V\,K^{-1}}$ and $S_s = 168.0\,\mu\mathrm{V\,K^{-1}}$.

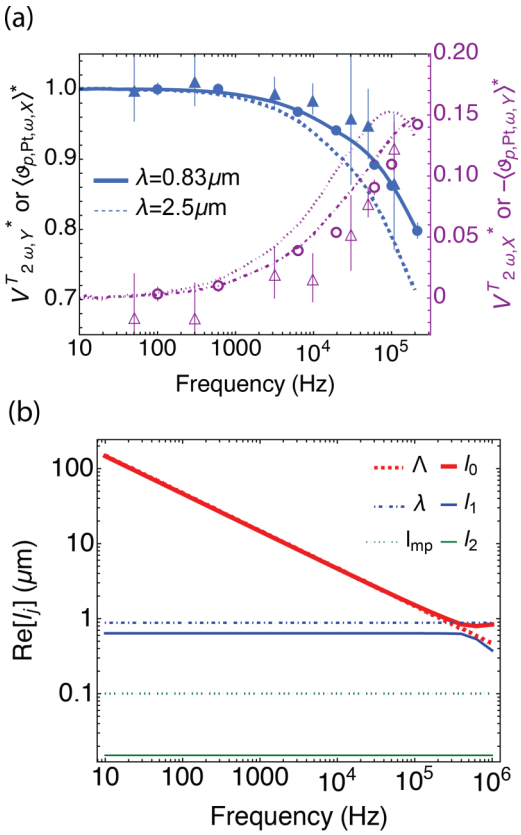

FIG. 4. (a) Comparison between the in-phase (filled symbols and thick blue lines, left axis) and out-of-phase (open symbols and thin purple lines, right axis) components of the normalized frequency-dependent 2ω SSE signals (circles) and 1ω SPE signals (triangles) with the analytical solutions for the SSE (solid lines) at $l_{mp} = 250$ nm and $\lambda = 0.83\,\mu$m (solid lines) or $\lambda = 2.5\,\mu$m (dashed lines). Frequency on the x axis equals $\frac{\omega}{2\pi}$ for SPE and $\frac{\omega}{\pi}$ for SSE. (b) Calculated $l_{j=0,1,2}$ at the 2ω frequency in comparison with Λ, $\lambda = 0.83\,\mu$m, and $l_{mp} = 250\,$nm.

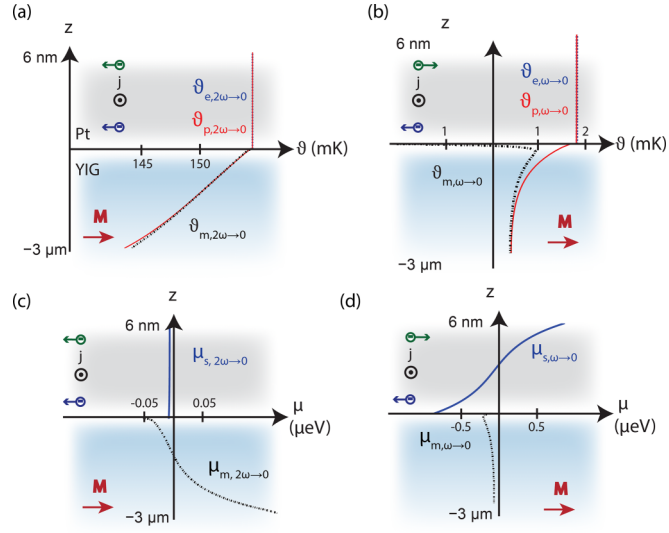

FIG. 5. Analytical solutions of 2ω (a), (c) and 1ω (b), (d) temperature and spin accumulation modulations for Pt electrons (ϑ_e, μ_s), Pt and YIG phonons (ϑ_p), and YIG magnons (ϑ_m, μ_m) at the low-frequency limit. In YIG, dotted and solid lines are for magnons and phonons, respectively. Calculations are based on the fitting parameters obtained from $\Delta V^{T}_{2\omega}$ fitting (Table S1).

of the measurement, λ and l_{mp} of our samples should be smaller than the Λ value of 1.5 μm of the 2ω component within the 10^5-Hz frequency range. This finding agrees with a prior report of a 1-μm-scale magnon propagation length in SSE measurements [33].

We find that our frequency-dependent SSE signal [Fig. 4(a)] can be fitted well with $\lambda = 0.83$ μm and $l_{mp} =$ 250 nm [24,25], magnon thermal conductivity $\kappa_M = 0.1$ $\mathrm{Wm^{-1}\,K^{-1}}$, $\sigma_m = 1.85 \times 10^6\,\mathrm{Sm^{-1}}$, $S_m = 63.5\,\mu\mathrm{V\,K^{-1}}$, and an interface spin Seebeck coefficient $S_s = 65.5\,\mu\mathrm{V\,K^{-1}}$. which yields the calculated temperature and μ_m profiles of Fig. 5 at the low-frequency limit. These and other properties used for the fitting are within one order of magnitude of prior reported theoretical and experimental estimates [28].The same values can also fit the observed frequency dependence of the normalized SPE signal. Based on our model, λ, instead of l_{mp} proposed in Ref. [30], controls the reported SSE dependences on the thickness and frequency [31], consistent with recent reports of relatively long λ values [23,34].

We note that the thermally injected magnons responsible for the 2ω SSE modulation are in a different frequency range compared to the magnons that are electrically injected by the SHE that give rise to the 1ω SPE modulation, as discussed in a recent work that shows different λ values for the thermally and electrically injected magnons [35]. Similarly, other transport properties are also expected to differ for the electrically injected and thermally injected magnons. Indeed, we find that a change of the fitting parameters to $S_m = 45\ \mu\mathrm{V\,K^{-1}}$ and $S_s = 168\ \mu\mathrm{V\,K^{-1}}$ can lead to satisfactory fitting of both the frequency dependence and magnitude of the measured SPE signal. It should be noted that spin-mediated interfacial heat transfer can also enable the transfer of Ettingshausen heat from Pt electrons to YIG magnons. However, the Ettingshausen effect does not produce the measured frequency dependence and can produce the magnitude of the observed low-frequency first-harmonic signal only when the Nernst coefficient is anomalously large. Additional discussions on this and other effects are included in the Supplemental Material [28] with additional references [36–47].

We compare our results with recently reported experimental data [21], which exceed their magnonic USMR prediction by about one order of magnitude at a modest $\boldsymbol{H}$ field that is comparable to ours. In addition, the TCR of their thinner Pt line is smaller than ours. Moreover, the SPE is expected to be reduced considerably in their samples with the YIG film thickness below 300 nm (see Fig. S14), much smaller than the micrometer-scale λ. Consequently, the SPMR is below the detection limit of their measurement technique. Similar reasons have also resulted in the undetectable SPMR contribution in the 90-nm YIG/3-nm Pt sample studied in an earlier work [20], where ∼ 90% of the measured 2ω signal was attributed to the SSE and the origin of the remaining 10% remains to be better understood.

Our measurements and analyses show that the UMR in HM/FI heterostructures is much larger than prior theories that have only considered the interfacial spin flux but not the spin-mediated heat flux caused by electron-magnon scattering. The reversal of magnetization, which is aligned with the spin accumulation, causes a small change in the magnitude of the interface spin flux injected by SHE due to the variation of magnon accumulation. However, it reverses the direction of the corresponding spin Peltier heat flux, resulting in a much larger UMR than expected from spin flux alone. By accounting for both magnon chemical potential and nonequilibrium magnon temperature, our analytical model shows that the frequency- and thickness-dependent SPE and SSE processes are caused by a reduction of either the thermal penetration depth or thickness to the micrometer-scale magnon spin-diffusion length instead of the submicrometer magnon-phonon thermalization length. The frequency-dependent measurements and analyses introduced here offer a unique probe of the fundamental length scales of spin and energy carriers and facilitate the exploration of nonequilibrium magnons as carriers of information and energy.

We thank David Cahill for helpful discussions and for sharing the Pt/YIG interface thermal conductance measurement data. We additionally thank Anthony Stauzenberger, Uttam Ghoshal, Yoonho Seo, and Neal Hall for providing assistance in sputter deposition of thin Pt films. This work was supported by the U.S. Army Research Office Multidisciplinary University Research Initiative (MURI) Grant No. W911NF-14-1-0016. H.L. was supported by the U.S. Office of Naval Research MURI Grant No. N00014-16-1-2436. L.S. carried out the angle-dependent measurements with assistance from Devika Mehta, Peter Sokalski, Yajie Huang, and Qianru Jia for instrumentation and data acquisition programs.

S.E.S., A.W., and L.S. designed and carried out the low-frequency measurements; H.L., L.S., and S.E.S. designed and carried out the high-frequency measurements; L.S. developed the analytical models; H.L. and S.E.S. carried out calculations. All authors contributed to the writing of the manuscript.

[1] H. Nakayama, M. Althammer, Y.-T. Chen, K. Uchida, Y. Kajiwara, D. Kikuchi, T. Ohtani, S. Geprägs, M. Opel, S. Takahashi *et al.*, Spin Hall Magnetoresistance Induced by a Nonequilibrium Proximity Effect, Phys. Rev. Lett. **110**, 206601 (2013).

[2] C. O. Avci, K. Garello, A. Ghosh, M. Gabureac, S. F. Alvarado, and P. Gambardella, Unidirectional spin Hall magnetoresistance in ferromagnet/normal metal bilayers, Nat. Phys. **11**, 570 (2015).

[3] S. Vélez, V. N. Golovach, A. Bedoya-Pinto, M. Isasa, E. Sagasta, M. Abadia, C. Rogero, L. E. Hueso, F. S. Bergeret, and F. Casanova, Hanle Magnetoresistance in Thin Metal Films with Strong Spin-Orbit Coupling, Phys. Rev. Lett. **116**, 016603 (2016).

[4] K. Uchida, H. Adachi, T. Ota, H. Nakayama, S. Maekawa, and E. Saitoh, Observation of longitudinal spin-Seebeck effect in magnetic insulators, Appl. Phys. Lett. **97**, 172505 (2010).

[5] J. Flipse, F. K. Dejene, D. Wagenaar, G. E. W. Bauer, J. Ben Youssef, and B. J. van Wees, Observation of the Spin Peltier Effect for Magnetic Insulators, Phys. Rev. Lett. **113**, 027601 (2014).

[6] S. Daimon, R. Iguchi, T. Hioki, E. Saitoh, and K. Uchida, Thermal imaging of spin Peltier effect, Nat. Commun. **7**, 13754 (2016).

[7] S. Daimon, K.-i. Uchida, R. Iguchi, T. Hioki, and E. Saitoh, Thermographic measurements of the spin Peltier effect in metal/yttrium-iron-garnet junction systems, Phys. Rev. B **96**, 024424 (2017).

[8] T. McGuire and R. Potter, Anisotropic magnetoresistance in ferromagnetic 3d alloys, IEEE Trans. Magn. **11**, 1018 (1975).

[9] G. Binasch, P. Grünberg, F. Saurenbach, and W. Zinn, Enhanced magnetoresistance in layered magnetic structures with antiferromagnetic interlayer exchange, Phys. Rev. B **39**, 4828 (1989).

[10] M. N. Baibich, J. M. Broto, A. Fert, F. Nguyen Van Dau, F. Petroff, P. Etienne, G. Creuzet, A. Friederich, and J. Chazelas, Giant Magnetoresistance of (001)Fe/(001)Cr Magnetic Superlattices, Phys. Rev. Lett. **61**, 2472 (1988).

[11] M. I. D'yakonov and V. I. Perel', Possibility of orienting electron spins with current, JETP Lett. **13**, 657 (1971).

[12] J. E. Hirsch, Spin Hall Effect, Phys. Rev. Lett. **83**, 1834 (1999).

[13] S. Murakami, N. Nagaosa, and S.-C. Zhang, Dissipationless quantum spin current at room temperature, Science **301**, 1348 (2003).

[14] Y. K. Kato, R. C. Myers, A. C. Gossard, and D. D. Awschalom, Observation of the spin Hall effect in semiconductors, Science **306**, 1910 (2004).

[15] C. O. Avci, J. Mendil, G. S. D. Beach, and P. Gambardella, Origins of the Unidirectional Spin Hall Magnetoresistance in Metallic Bilayers, Phys. Rev. Lett. **121**, 087207 (2018).

[16] S. S.-L. Zhang and G. Vignale, Theory of unidirectional spin hall magnetoresistance in heavy-metal/ferromagnetic-metal bilayers, Phys. Rev. B **94**, 140411(R) (2016).

[17] S. Langenfeld, V. Tshitoyan, Z. Fang, A. Wells, T. A. Moore, and A. J. Ferguson, Exchange magnon induced resistance asymmetry in permalloy spin-Hall oscillators, Appl. Phys. Lett. **108**, 192402 (2016).

[18] W. P. Sterk, D. Peerlings, and R. A. Duine, Magnon contribution to unidirectional spin Hall magnetoresistance in ferromagnetic-insulator/heavy-metal bilayers, Phys. Rev. B **99**, 064438 (2019).

[19] J. Xiao, G. E. W. Bauer, K.-c. Uchida, E. Saitoh, and S. Maekawa, Theory of magnon-driven spin Seebeck effect, Phys. Rev. B **81**, 214418 (2010).

[20] C. O. Avci, K. Garello, J. Mendil, A. Ghosh, N. Blasakis, M. Gabureac, M. Trassin, M. Fiebig, and P. Gambardella, Magnetoresistance of heavy and light metal/ferromagnet bilayers, Appl. Phys. Lett. **107**, 192405 (2015).

[21] G. Liu, X.-g. Wang, Z. Z. Luan, L. F. Zhou, S. Y. Xia, B. Yang, Y. Z. Tian, G.-h. Guo, J. Du, and D. Wu, Magnonic Unidirectional Spin Hall Magnetoresistance in a Heavy-Metal–Ferromagnetic-Insulator Bilayer, Phys. Rev. Lett. **127**, 207206 (2021).

[22] M. Schreier, A. Kamra, M. Weiler, J. Xiao, G. E. W. Bauer, R. Gross, and S. T. B. Goennenwein, Magnon, phonon, and electron temperature profiles and the spin Seebeck effect in

magnetic insulator/normal metal hybrid structures, Phys. Rev. B **88**, 094410 (2013).

[23] L. J. Cornelissen, K. J. H. Peters, G. E. W. Bauer, R. A. Duine, and B. J. van Wees, Magnon spin transport driven by the magnon chemical potential in a magnetic insulator, Phys. Rev. B **94**, 014412 (2016).

[24] A. Prakash, B. Flebus, J. Brangham, F. Yang, Y. Tserkovnyak, and J. P. Heremans, Evidence for the role of the magnon energy relaxation length in the spin Seebeck effect, Phys. Rev. B **97**, 020408(R) (2018).

[25] J. S. Jamison, Z. Yang, B. L. Giles, J. T. Brangham, G. Wu, P. C. Hammel, F. Yang, and R. C. Myers, Long lifetime of thermally excited magnons in bulk yttrium iron garnet, Phys. Rev. B **100**, 134402 (2019).

[26] N. Vlietstra, J. Shan, V. Castel, J. Ben Youssef, G. E. W. Bauer, and B. J. van Wees, Exchange magnetic field torques in YIG/Pt bilayers observed by the spin-Hall magnetoresistance, Appl. Phys. Lett. **103**, 032401 (2013).

[27] H. Wang, C. Du, P. C. Hammel, and F. Yang, Comparative determination of $Y_3Fe_5O_{12}$/Pt interfacial spin mixing conductance by spin-Hall magnetoresistance and spin pumping, Appl. Phys. Lett. **110**, 062402 (2017).

[28] See Supplemental Material at http://link.aps.org/supplemental/10.1103/PhysRevB.107.L140412 for details of experimental methods and analytical models.

[29] R. Itoh, R. Iguchi, S. Daimon, K. Oyanagi, K.-i. Uchida, and E. Saitoh, Magnetic-field-induced decrease of the spin Peltier effect in Pt/$Y_3Fe_5O_{12}$ system at room temperature, Phys. Rev. B **96**, 184422 (2017).

[30] Y. Xu, W. Zhao, and S. Mangin, Frequency dependence of the longitudinal spin Seebeck effect, Phys. Rev. B **98**, 144408 (2018).

[31] M. Schreier, F. Kramer, H. Huebl, S. Geprägs, R. Gross, S. T. B. Goennenwein, T. Noack, T. Langner, A. A. Serga, B. Hillebrands, and V. I. Vasyuchka, Spin Seebeck effect at microwave frequencies, Phys. Rev. B **93**, 224430 (2016).

[32] C. Du, T. van der Sar, T. X. Zhou, P. Upadhyaya, F. Casola, H. Zhang, M. C. Onbali, C. Ross, R. L. Walsworth, Y. Tserkovnyak, and A. Tacoby, Control and local measurement of the spin chemical potential in a magnetic insulator, Science **357**, 195 (2017).

[33] A. Kehlberger, U. Ritzmann, D. Hinzke, E.-J. Guo, J. Cramer, G. Jakob, M. Onbasli, D. H. Kim, C. A. Ross, M. B. Jungfleisch *et al.*, Length Scale of the Spin Seebeck Effect, Phys. Rev. Lett. **115**, 096602 (2015).

[34] K. An, K. S. Olsson, A. Weathers, S. Sullivan, X. Chen, X. Li, L. G. Marshall, X. Ma, N. Klimovich, J. Zhou, L. Shi, and X. Q. Li, Magnons and Phonons Optically Driven out of Local Equilibrium in a Magnetic Insulator, Phys. Rev. Lett. **117**, 107202 (2016).

[35] J. M. Gomez-Perez, S. Vélez, L. E. Hueso, and F. Casanova, Differences in the magnon diffusion length for electrically and thermally driven magnon currents in $Y_3Fe_5O_{12}$, Phys. Rev. B **101**, 184420 (2020).

[36] M. I. Dyakonov, Magnetoresistance due to Edge Spin Accumulation, Phys. Rev. Lett. **99**, 126601 (2007).

[37] V. E. Demidov, S. Urazhdin, B. Divinskiy, V. D. Bessonov, A. B. Rinkevich, V. V. Ustinov, and S. O. Demokritov, Chemical potential of quasi-equilibrium magnon gas driven by pure spin current, Nat. Commun. **8**, 1579 (2017).

[38] S. R. Boona and J. P. Heremans, Magnon thermal mean free path in yttrium iron garnet, Phys. Rev. B **90**, 064421 (2014).

[39] A. M. Hofmeister, Thermal diffusivity of garnets at high temperature, Phys. Chem. Miner. **33**, 45 (2006).

[40] K. Uchida, T. Kikkawa, A. Miura, J. Shiomi, and E. Saitoh, Quantitative Temperature Dependence of Longitudinal Spin Seebeck Effect at High Temperatures, Phys. Rev. X **4**, 041023 (2014).

[41] C. Euler, P. Hołuj, T. Langner, A. Kehlberger, V. I. Vasyuchka, M. Kläui, and G. Jakob, Thermal conductance of thin film YIG determined using Bayesian statistics, Phys. Rev. B **92**, 094406 (2015).

[42] Z. Lin, L. V. Zhigilei, and V. Celli, Electron-phonon coupling and electron heat capacity of metals under conditions of strong electron-phonon nonequilibrium, Phys. Rev. B **77**, 075133 (2008).

[43] J. Barker and G. E. W. Bauer, Semiquantum thermodynamics of complex ferrimagnets, Phys. Rev. B **100**, 140401 (2019).

[44] M. Weiler, M. Althammer, M. Schreier, J. Lotze, M. Pernpeintner, S. Meyer, H. Huebl, R. Gross, A. Kamra, J. Xiao *et al.*, Experimental Test of the Spin Mixing Interface Conductivity Concept, Phys. Rev. Lett. **111**, 176601 (2013).

[45] L. J. Cornelissen, J. Liu, R. A. Duine, J. B. Youssef, and B. J. van Wees, Long-distance transport of magnon spin information in a magnetic insulator at room temperature, Nat. Phys. **11**, 1022 (2015).

[46] X.-Y. Wei, O. A. Santos, C. H. S. Lusero, G. E. W. Bauer, J. Ben Youssef, and B. J. van Wees, Giant magnon spin conductivity in ultrathin yttrium iron garnet films, Nat. Mater. **21**, 1352 (2022).

[47] E.-J. Guo, J. Cramer, A. Kehlberger, C. A. Ferguson, D. A. MacLaren, G. Jakob, and M. Kläui, Influence of Thickness and Interface on the Low-Temperature Enhancement of the Spin Seebeck Effect in YIG Films, Phys. Rev. X **6**, 031012 (2016).